Received: 4 October 2021 | Revised: 12 January 2022 | Accepted: 17 January 2022

DOI: 10.1002/bio.4200

RESEARCH ARTICLE

LUMINESCENCE WILEY
The Journal of Biological and Chemical Luminescence

Study on luminescence properties of Ce^{3+} and Eu^{3+} ions in a nanocrystalline hexagonal $Zn_4Al_{22}O_{37}$ novel system

Dinesh S. Bobade[1,3] | **Yatish R. Parauha**[2] | **Sanjay J. Dhoble**[2] | **Prabhakar B. Undre**[3]

[1]Department of Physics, RNC Arts, JDB Commerce and NSC Science College, Nashik, Maharashtra, India

[2]Department of Physics, Rashtrasant Tukdoji Maharaj Nagpur University, Nagpur, Maharashtra, India

[3]Department of Physics, Dr. Babasaheb Ambedkar Marathwada University, Aurangabad, Maharashtra, India

Correspondence
Dinesh S. Bobade and Prabhakar B. Undre, Department of Physics, Dr. Babasaheb Ambedkar Marathwada University, Aurangabad, Maharashtra, India.
Email: dsbobade1104@gmail.com; prabhakarundre@yahoo.co.in.

Abstract

The present communication is strongly focused on the investigation of synthesis, structural and luminescence properties of cerium (Ce^{3+})- and europium (Eu^{3+})-activated $Zn_4Al_{22}O_{37}$ phosphors. Ce^{3+}- and Eu^{3+}-doped $Zn_4Al_{22}O_{37}$ novel phosphors were prepared using a solution combustion synthesis route. Structural properties were studied using powder X-ray diffraction and high-resolution transverse electron microscopy. The optical properties were studied using ultraviolet–visible light spectroscopy and Fourier transform infrared spectroscopy; luminescence properties were studied using a photoluminescence (PL) technique. The crystal structure of the prepared $Zn_4Al_{22}O_{37}$ host and Ce^{3+}- and Eu^{3+}-activated $Zn_4Al_{22}O_{37}$ phosphors was investigated and was found to have a hexagonal structure. The measured PL emission spectrum of the Ce^{3+}-doped $Zn_4Al_{22}O_{37}$ phosphor showed an intense and broad emission band centred at 421 nm under a 298 nm excitation wavelength. By contrast, the Eu^{3+}-doped $Zn_4Al_{22}O_{37}$ phosphor exhibited two strong and intense emission bands at approximately 594 nm (orange) and 614 nm (red), which were monitored under 395 nm excitation. The Commission Internationale de l'Eclairage (CIE) colour coordinates of the Ce^{3+}-doped $Zn_4Al_{22}O_{37}$ were investigated and found to be $x = 0.1567$, $y = 0.0637$ (blue) at 421 nm and for Eu^{3+}-doped $Zn_4Al_{22}O_{37}$ were $x = 0.6018$, $y = 0.3976$ (orange) at 594 nm and $x = 0.6779$, $y = 0.3219$ (red) at 614 nm emission. The luminescence behaviour of the synthesized phosphors suggested that these phosphors may be used in lighting applications.

KEYWORDS
FT-IR, HR-TEM, nanophosphor, PL, UV, XRD

1 | INTRODUCTION

Rare earth element-activated phosphors have been used on a large scale in different fields in light emission industries due to their specific characteristics of emission in the visible and near-visible light regions. These rare earths have been widely used as activators in different systems due to their high fluorescence efficiency in which the size of their particles is reduced to the nanoscale level. The different applications of rare earth activated materials are for example fluorescence lamps, cathode-ray tubes, light-emitting diodes (LEDs) for the lighting industry, field-emission displays, and X-ray imaging.[1–6] Ce^{3+}- and Eu^{3+}-activated luminescence materials have attracted the attention of the researchers due to their high lumen output and characteristic emission properties in the visible and near-visible light regions. These Ce^{3+}- and Eu^{3+}-activated luminescence materials have attracted much interest due to their expected luminescence properties. Different types of activator-based luminescence materials such as aluminates, chlorides, nitrides, silicates, borates, phosphates, oxy-nitrides,

 © 2022 John Wiley & Sons Ltd.

etc. have been prepared and applied in the field of luminescence[7,8] Among these, aluminates have demonstrated more advantages such as high luminous efficiency, excellent durability, and low cost, and good physical and chemical stability.[9–11]

Ce^{3+}-doped materials have attracted more interest because their spin and parity allow optical 4f→5d transitions, which have fast radiative lifetimes of ∼10–50 nsec,[6] which is desirable for application in scintillators, LEDs, and field-emission displays. Recently, significant efforts have been made by several research groups on the synthesis and study of various Ce^{3+}-doped fluoride and oxide materials.[12–14] The first white LED was commercialized by the Nichia Company,[15] in which a blue LED was coated with the yellowish phosphor YAG:Ce. The Ce^{3+}-doped $CaAl_{12}O_{19}$, $CaAl_4O_7$, $SrAl_4O_7$, and $SrAl_{12}O_{19}$ samples demonstrated a promising broad emission band that was centred at 355, 320, 330, and 317 nm, respectively. These host crystal structures had great influence on the prominent emission peaks of aluminate-based phosphors.[15] The photoluminescence (PL) emission spectra of the $LiAl_5O_8$ and $NaAl_{11}O_{17}$ phosphors were studied by Nikhare *et al.*[16] and strong Ce^{3+} emission was observed at ∼310 nm for the excitation at a wavelength of 254 nm due to the 5d→4f transition.

The emission of Eu^{3+}-doped phosphors revealed maximum intensities at 580 nm (j = 0), 592 nm (j = 1), 618 nm (j = 2), 650 nm (j = 3), and 690 nm (j = 4) because of the transition from minimum excited state of $^5D_0$ to different ^7F_j (j = 0 to 4). Ideally, weak emissions corresponding to the transition of j = 1, 4, and 5 are observed, whereas red emission at 613 nm and orange emission at 592 nm are seen as dominant. These transitions were strongly influenced by the symmetry acquired by the Eu^{3+} ion and the nature of its surrounding area.[17–19] The red emission at ∼614 nm was attributed to the $^5D_0 \rightarrow {}^7F_2$ transition corresponding to the electric dipole transition and orange emission at ∼591 nm that belonged to the $^5D_0 \rightarrow {}^7F_1$ transition corresponding to a magnetic dipole transition.[20] Kim[21] noted that the transition for $^5D_0 \rightarrow {}^7F_1$ levels at 590 nm was attributed to the Eu^{3+} ion acquired at the symmetrical sites in the crystal, there was also another low intensity peak observed at 610 nm due to Eu^{3+} ions that acquired low symmetry sites in the crystal. Other emission peaks located at 654 nm and 701 nm were attributed to the transitions from $^5D_0 \rightarrow {}^7F_3$ and $^7F_4$ levels, respectively.

As far as rare earth ion-doped zinc aluminates are concerned, a lack of study was observed in systems other than the $ZnAl_2O_4$ system. $ZnAl_2O_4$ has been widely studied and its structural, optical, and electronic properties have been investigated by several researchers.[9–11,22,23] Several investigations have been devoted to incorporating rare earth elements and transition metal ions into the $ZnAl_2O_4$ system.[24–27] Different trivalent rare earth ions such as Dy^{3+}, Tb^{3+}, and Eu^{3+} have been incorporated into $ZnAl_2O_4$ for display applications.[25,28,29] As a result, ultraviolet (UV) photoelectronic devices can be made with $ZnAl_2O_4$.[30,31] Kumar *et al.*[32] investigated a Sm^{3+}-activated $ZnAl_2O_4$ phosphor preparation for characterization and photoluminescence. The luminous and X-ray photoelectron characteristics of $ZnAl_2O_4$:Ce^{3+},Tb^{3+} phosphor were investigated by Tshabalala *et al.*[33]

No attempt, so far, seems to have been made to study other systems in zinc aluminates. The aim of this investigation was to prepare and study the structural and luminescence properties of Ce^{3+}- and Eu^{3+}-activated $Zn_4Al_{22}O_{37}$ phosphors. The samples were prepared using solution combustion synthesis and urea was used as a fuel agent to enhance the combustion. These samples were characterized using X-ray diffraction (XRD), high-resolution transverse electron (HR-TEM) microscopy, UV–visible (UV–vis) light spectroscopy, Fourier transform infrared (FT-IR) spectroscopy and photoluminescence (PL) techniques.

2 | EXPERIMENTAL

2.1 | Sample preparation

Combustion synthesis is one of the easiest, simplest, and large-scale applicable methods for the synthesis of the crystalline and nanostructured materials. Ce^{3+}- and Eu^{3+}-doped $Zn_4Al_{22}O_{37}$ phosphors were prepared by solution combustion using high purity analytical reagent (AR) grade compounds $(ZnNO_3)_2.6H_2O$, $Al(NO_3)_3.9H_2O$, $(NH_4)_2NO_3$, $Ce(NO_3)_3.9H_2O$, Eu_2O_3 and nitric acid as initial raw materials and urea was used as the fuel agent to enhance combustion. All precursors were weighed precisely at a stoichiometric ratio and dissolved in 20 ml distilled water. The solution was stirred for 30 min using a magnetic stirrer to acquire a homogeneous solution. Next, it was placed in a muffle furnace that was maintained at 500°C temperature. The solution was boiled to evolve the gases and created combustion within 5–8 min. By the end of combustion foamy powder samples were formed. The temperature of the solution reached almost 1400°C during combustion and, due to this, nanocrystalline samples were obtained. The prepared powder samples were characterized to investigate the different properties.

2.2 | Characterization

A phase and structural study of $ZnAl_{12}O_{19}$ was carried out using XRD (Bruker D8 Advance) with Cu $K_{\alpha 1}$ irradiation (λ = 1.5406 Å) and operating at 40 kV, 30 mA over the 2θ range 10–80°. A topography and morphology study of $Zn_4Al_{22}O_{37}$ was carried out using HR-TEM (FEI Titan 80–300 TEM). The optical properties (band gaps) were measured using UV–vis spectrophotometry (Shimadzu, Japan) and the luminescence properties are studied using a PL spectrophotometer (Perkin Elmer).

3 | RESULTS AND DISCUSSION

3.1 | X-ray diffraction analysis

The structural properties of the prepared samples were estimated using an XRD technique. Figure 1 shows the powder XRD patterns of

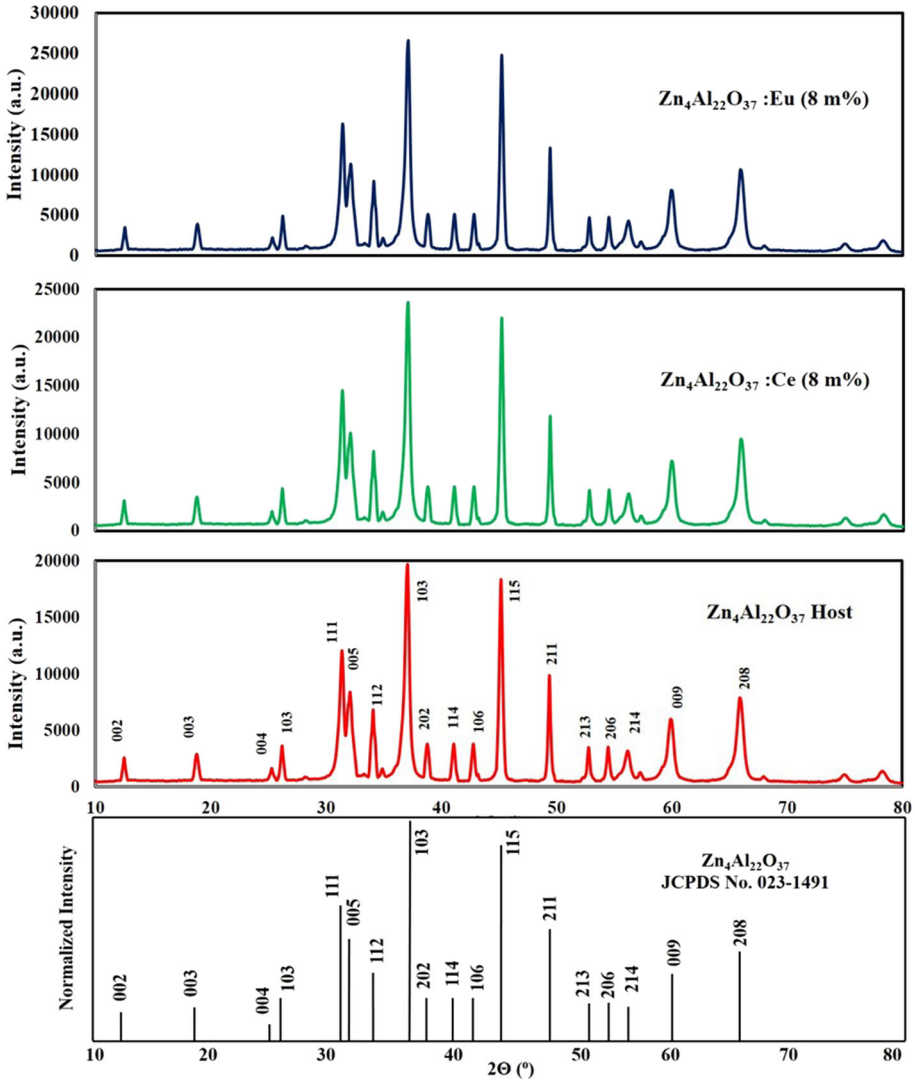

FIGURE 1 X-ray powder diffraction patterns of pure $Zn_4Al_{22}O_{37}$, Ce^{3+}-activated $Zn_4Al_{22}O_{37}$ and Eu^{3+}-activated $Zn_4Al_{22}O_{37}$ phosphors and standard JCPDS file for $Zn_4Al_{22}O_{37}$

(a) host $Zn_4Al_{22}O_{37}$, (b) 0.8 m% Ce^{3+}-activated $Zn_4Al_{22}O_{37}$, and (c) 0.8 m% Eu^{3+}-activated $Zn_4Al_{22}O_{37}$ phosphor taken at a 0.05°/s scanning rate in the range 20–80°.

The determination of lattice parameters is a very time-consuming task and sometimes it is easy to match hkl values with the $\sin^2\theta$. While indexing the 2θ values, some peaks of less intensity might be omitted, then the actual indexing may affect the *hkl* values (Miller indices). Therefore, for hexagonal structures, the analytical method is used to calculate the lattice parameters. Using Bragg's diffraction condition and the interplanar distance, we could obtain the equation for $\sin^2\theta$ as:

$$\sin^2\theta = \frac{\lambda^2}{4a^2}\left[\frac{4}{3}\left(h^2+hk+l^2\right)+\frac{l^2}{(c/a)^2}\right] \quad (1)$$

where $\sin^2\theta$ values can be calculated using the lattice parameters *a*, *c*, and the *hkl* values. For given structure the lattice parameters *a* and *c* are constants, then the $\sin^2\theta$ values depend upon *h*, *k*, and *l*. The above Equation (1) was converted into simplified form as:

$$\sin^2\theta = A\left(h^2+hk+k^2\right)+Cl^2 \quad (2)$$

where $A=\frac{\lambda^2}{3a^2}$, $C=\frac{\lambda^2}{4c^2}$ and *hkl* are integers. The values of h^2+hk+k^2 were obtained by choosing $l=0$ and then A was calculated. The value C was calculated from the equation $h^2+hk+k^2=0$ and choosing the values of $l=0$, 1, 2, 3, 4, etc. The constant C was calculated using the following equation:

$$Cl^2 = \sin^2\theta - A\left(h^2+hk+k^2\right) \quad (3)$$

The values of the lattice parameters *a* and *c* were estimated using A and C (constants) and other Miller indices were estimated using Equation (1). The Miller indices corresponding to high intensity peaks are listed in Table 1. The lattice parameters were calculated and these were $a = 5.6790$, $c = 13.7100$, $\alpha = 90°$, $\beta = 90°$ and $\gamma = 120°$. Also structure calculations were carried out using Endeavour software and estimated atomic positions of the prepared $Zn_4Al_{22}O_{37}$ are given in Table 2.

TABLE 1 Crystallite size calculation of $Zn_4Al_{22}O_{37}$

Sr. no.	2 θ(°)	d (Å)	FWHM	Crystallite size (nm)	Miller indices (*hkl*)
1	12.5	7.0754	0.3028	26.08	002
2	18.8	4.7162	0.3873	20.23	010
3	25.3	3.5173	0.4054	19.12	400
4	26.2	3.3985	0.342	22.62	013
5	28.2	3.1618	0.6622	11.63	110
6	31.4	2.8465	0.5123	14.92	014
7	32.1	2.7860	0.6206	12.30	111
8	32.6	2.7420	0.3472	21.96	005
9	34.19	2.6201	0.3943	19.47	112
10	37.1	2.4212	0.5199	14.48	113
11	38.8	2.3189	0.294	25.48	022
12	41.1	2.1943	0.3419	21.75	114
13	42.8	2.1110	0.3517	21.03	106
14	45.2	2.0043	0.3905	18.78	115
15	49.4	1.8433	0.3704	19.48	121
16	52.8	1.7323	0.4323	16.46	008
17	54.5	1.6822	0.3661	19.29	213
18	56.2	1.6353	0.5607	12.49	124
19	57.3	1.6065	0.5187	13.44	117
20	59.9	1.5428	0.6124	11.24	009
21	65.9	1.4161	0.6746	9.88	208
22	68	1.3774	0.2667	24.69	222
23	75	1.2653	0.6074	10.37	314
24	78.3	1.2200	0.9348	6.59	400

The prominent diffracted intensity peaks with *hkl* values are shown in Figure 1. High intensity peaks were observed for the prepared samples, which denoted the highly crystalline nature of the samples. The XRD pattern peaks of the synthesized samples were well matched with the standard Joint Committee on Powder Diffraction Standards (JCPDS) file no. 23-1491 of $Zn_4Al_{22}O_{37}$, as shown in Figure 1. In the diffraction patterns, no impurity peak was observed, which indicated that the dopants Ce^{3+} and Eu^{3+} were well incorporated in the host $Zn_4Al_{22}O_{37}$.

The crystallite size (D) was calculated using Debye–Scherer formula given below:

$$D = \frac{0.9\lambda}{\beta\cos\theta} \quad (4)$$

where, D is the crystallite size, 0.9 is the particle shape factor, λ is the wavelength of incident X-rays, β is the full width at half maximum (FWHM) of the *hkl* reflection and θ is the Bragg diffraction angle of the *hkl* reflection. The crystallite size for each *hkl* reflection was calculated and was observed in the 6.6–26 nm range, as shown in Table 2. The average crystallite size of pure $Zn_4Al_{22}O_{37}$ was determined to be 17 nm.

Atomic visualization is done by using Vesta software and it is shown in Figure 3. The hexagonal structure (space group P-6) was characterized as having close-packed arrays of oxygen atoms with polyhedral sites occupied by heterovalent cations. The different atomic structures of $Zn_4Al_{22}O_{37}$ unit cell are shown in Figure 3. The structure is of type $A_4B_{22}C_{37}$ and its atomic positions are presented in Table 2.

The coordination diagram with the ball-and-stick model is shown in Figure 2(a), which denotes that the Zn and Al atoms were coordinated by the oxygen atoms. These Zn and Al atoms occupied the central positions of the different polyhedral geometries, as shown in Figure 2(b). In this unit cell, the Zn atom had an ionic radius of 0.60 Å and its maximum coordinated number was observed to be 6. The Al atom hadan ionic radius of 0.54 Å and its coordinated eight oxygen atoms had ionic radii of 1.02 Å. The different lattice planes are shown in Figure 2(c–f) and this animation was created using Vesta software.

3.2 | High-resolution transmission electron spectroscopy analysis

HR-TEM technique is a very powerful tool to study of morphology, surface topography, crystal structure, and chemical composition of materials. The high energetic electron beam is diffracted through the sample and carries the structural and morphological information

TABLE 2 Atomic parameters of $Zn_4Al_{22}O_{37}$

Sr.no.	Atom	Oxidation state	Wyckoff positions	Atomic positions		
				x	y	z
1	Zn1	2	2*i*	0.6666	0.3333	0.42179
2	Zn2	2	1*d*	0.3333	0.6666	0.5000
3	Al1	3	3*j*	0.0796	0.6166	0
4	Al2	3	6 *L*	0.6632	0.0041	0.3249
5	Al3	3	6 *L*	0.4106	0.0369	0.1391
6	Al4	3	2 *g*	0	0	0.26991
7	Al5	3	2 *h*	0.3333	0.6666	0.2248
8	O1	−2	2*i*	0.6666	0.3333	0.1409
9	O2	−2	6 *L*	0.0155	0.5195	0.2362
10	O3	−2	6 *L*	0.1280	0.2786	0.3917
11	O4	−2	6 *L*	0.2375	0.0891	0.2076
12	O5	−2	3*j*	0.3986	0.0854	0
13	O6	−2	6 *L*	0.244	0.4001	0.0947
14	O7	−2	3 *k*	0.4011	0.00982	0.5
15	O8	−2	2*i*	0.6666	0.3333	0.3160
16	Zn3	2	1*b*	0	0	0.5
17	Al6	3	2 *g*	0	0	0.1039
18	Al7	3	1*e*	0.6666	0.3333	0
19	O9	−2	2 *h*	0.3333	0.6666	0.3261
20	O10	−2	1*a*	0	0	0

of the sample. The transmitted and diffracted beams are captured and diffraction pattern images for the prepared $Zn_4Al_{22}O_{37}$ are shown in Figure 3(a). The bright spots of atoms in concentric circles are clearly seen in the pattern. The interplanar distances for each ring were calculated in real space and these were observed to be consistent with the interplanar distance obtained using the XRD technique. The particle size was calculated using the HR-TEM image, as shown in Figure 3(b). The particle size was calculated using ImageJ software and was found to be a 20 nm average in size. Figure 3(c) shows the graph of the particle size calculation histogram. The surface topography images were captured at different areas, as shown in Figure 4. The d spacings between the crystallographic planes were estimated at different regions of the image in Figure 4(a) and corresponding *hkl* planes are shown in Figure 4(b–f). The lattice fringe width or d-spacing was calculated using ImageJ software. The scale of the image was calibrated using the straight line tool. The different regions were selected using the rectangle tool and the image was cropped. Then, the fast Fourier transform (FFT) process was carried out to find the position of the brightest point in the inverse lattice. The inverse FFT value was taken and then, by adjusting the threshold, the lattice fringes appeared in the image. These fringes from the different regions are shown in Figure 4(b–f). The lattice spacing was calculated using the plot profile. In the plot profile, by counting the number of peaks in a certain length, the lattice spacing is calculated.

3.3 | Ultraviolet–visible spectroscopy analysis

In most optical characterization techniques, the samples are bombarded with different types of radiation to study the different characteristics of the samples. UV–vis spectroscopy characterization is one of these techniques. In UV–vis spectroscopy the material is irradiated with UV–vis photons and emerging radiation is collected and data are constructed. Figure 5 demonstrates the UV–vis absorbance spectra of the Ce^{3+}- and Eu^{3+}-activated $Zn_4Al_{22}O_{37}$ and host $Zn_4Al_{22}O_{37}$. The band gap was modified by doping with Ce^{3+} and Eu^{3+} into $Zn_4Al_{22}O_{37}$. A blue shift occurred in the absorbance edge due to doping with Ce^{3+} and Eu^{3+} into the $Zn_4Al_{22}O_{37}$ system. From the UV–vis absorbance spectra, it is seen that the band gap energy of the host $Zn_4Al_{22}O_{37}$ decreased following Ce^{3+} doping in it. Incorporation of Ce^{3+} and Eu^{3+} ions into the $Zn_4Al_{22}O_{37}$ host created the discrete energy levels of Ce^{3+} and Eu^{3+} in the energy band gap of the host $Zn_4Al_{22}O_{37}$. When the Ce^{3+}- and Eu^{3+} ion-doped $Zn_4Al_{22}O_{37}$ phosphor was excited by UV–vis irradiation, then less energy was required for the excitation of the valence band electrons because of the decrease in the separation between the highest occupied and lowest unoccupied levels. The absorbance spectra consisted of an absorption band near 200 nm observed in both doped and undoped phosphor and related to the host material due to the characteristic transitions from metal–oxygen (Zn–O or Al–O) bands. A broad band was observed at 298 nm due to the

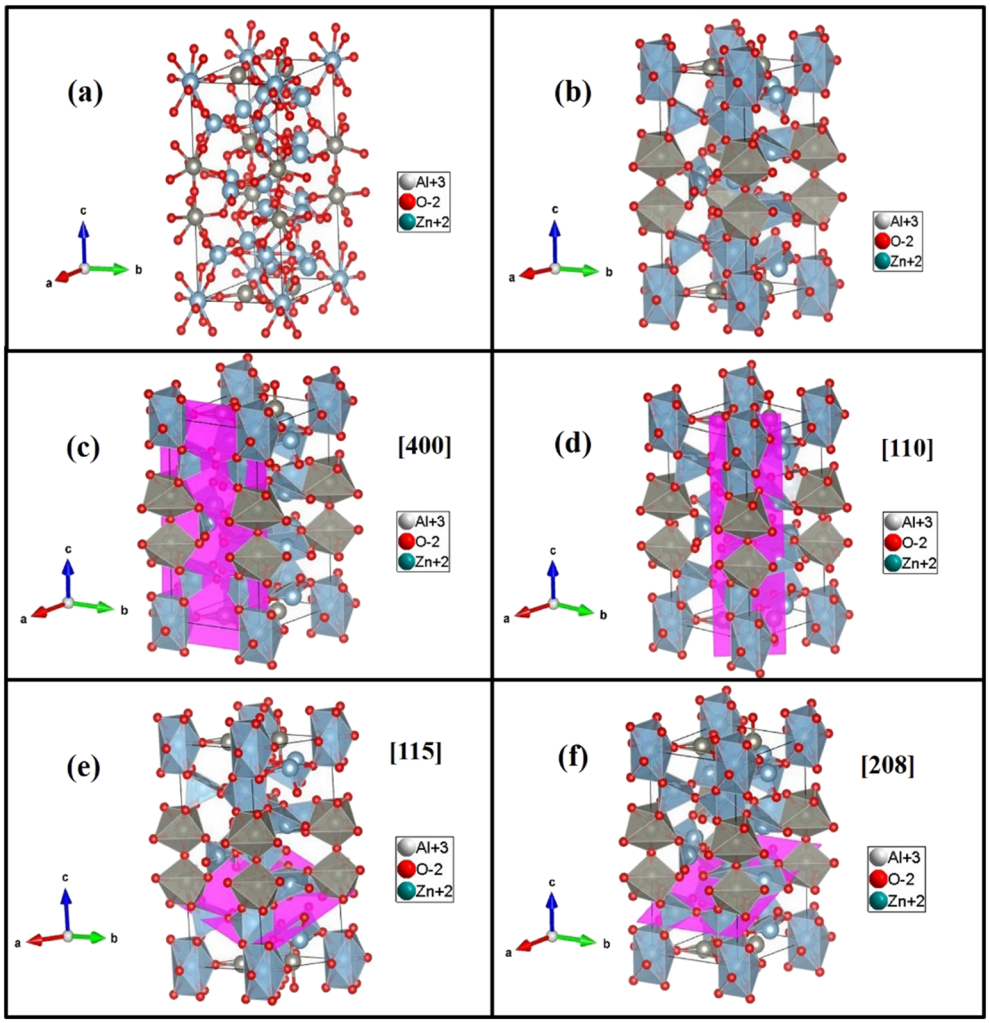

FIGURE 2 (a) Coordination ball-and-stick model of the $Zn_4Al_{22}O_{37}$ unit cell. (b) Polyhedral model of the $Zn_4Al_{22}O_{37}$ unit cell. (c–f) Different lattice planes (*hkl*) of the $Zn_4Al_{22}O_{37}$ unit cell

Ce–O band and a small shoulder peak was observed at 374 nm due to the Eu–O band.

Using the absorbance spectra, band gaps were calculated for pure and Ce^{3+}- and Eu^{3+}-activated $Zn_4Al_{22}O_{37}$ based on Kubelka–Munk theory.[34] To determine an optical energy gap, the Tauc plot approach was used. The Tauc equation was used to determine the optical band gap as given below:

$$\alpha = \frac{C(h\nu - E_g)^n}{h\nu} \quad (5)$$

where, α is the absorption coefficient, h is Plank's constant, ν is photon frequency, C is a constant, and Eg is the optical energy gap.[35] In the Tauc equation, the power n is a constant related to different types of electronic transitions (n = 1/2, 2, 3/2, or 3 for directly allowed, indirectly allowed, directly forbidden, and indirectly forbidden transitions, respectively). The curves in Figure 6 exhibited nonlinear and linear parts that denoted the characteristics of the directly allowed transitions. Therefore, in the Tauc equation the value of n was chosen as ½, then Equation (5) becomes:

$$(\alpha h\nu)^2 = A(h\nu - E_g) \quad (6)$$

The optical band gaps were calculated by plotting an $(\alpha h\nu)^2$ versus hν graph, the values of Eg were obtained by extrapolating the linearly fitted curves to $(\alpha h\nu)^2 = 0$. The optical band gap energies of pure $Zn_4Al_{22}O_{37}$, Ce^{3+}-activated $Zn_4Al_{22}O_{37}$, and Eu^{3+}-activated $Zn_4Al_{22}O_{37}$ were calculated and these were 4.13 eV, 3.33 eV, and 3.82 eV, respectively.

3.4 | Fourier transform infrared analysis

FT-IR spectroscopy was used to study molecular bonding and the strength of organic materials as well as inorganic materials. This technique measures the absorption/transmission of infrared radiation from a material by varying the wavenumber. FT-IR absorption bands identify molecular compositions and the structures of the samples. The molecules in the material absorb the incident infrared radiation and vibrate with a characteristic energy. This energy corresponds to

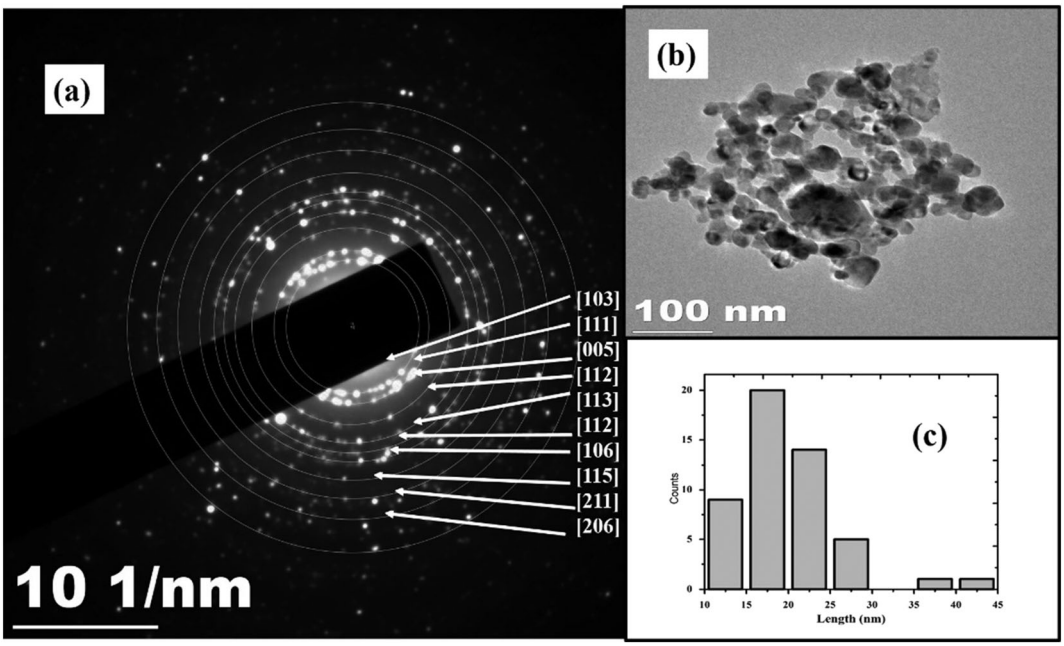

FIGURE 3 (a) Electron diffraction pattern for $Zn_4Al_{22}O_{37}$ using high-resolution transmission electron microscopy (HR-TEM). (b) HR-TEM image of $Zn_4Al_{22}O_{37}$. (c) Particle size calculation histogram

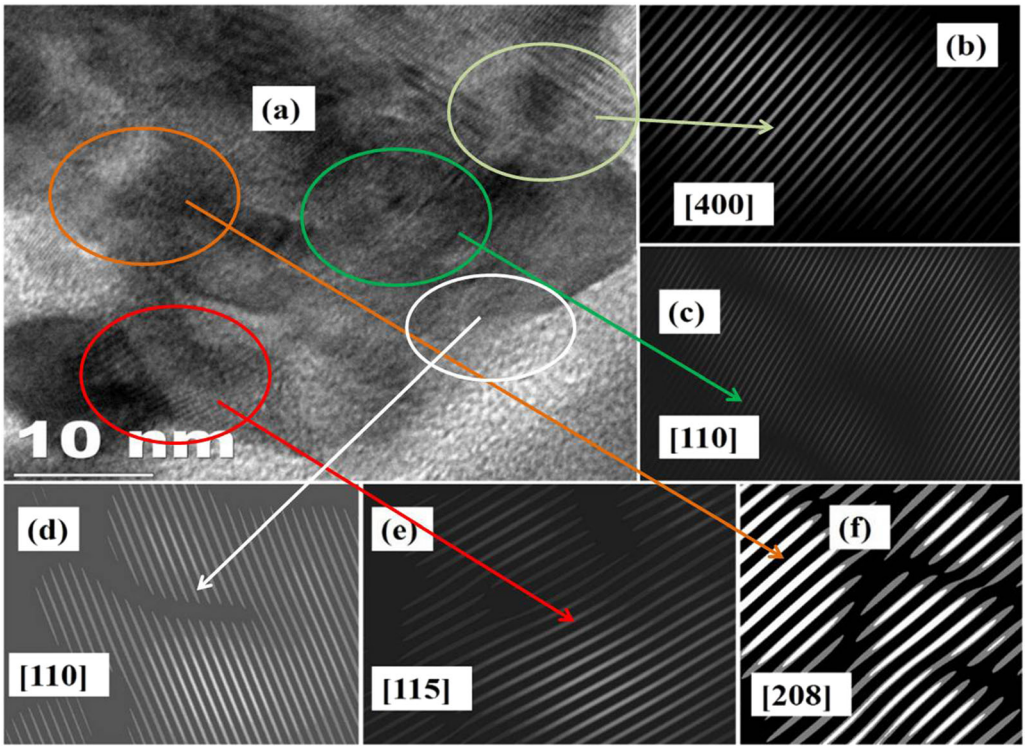

FIGURE 4 (a–f) Lattice planes of $Zn_4Al_{22}O_{37}$

the molecular structure of the material. In this technique, data are represented in terms of the intensity versus the wavenumber (cm^{-1}). The intensity is expressed in terms of the percentage of light absorbance or transmittance of each wavenumber.

Figure 7 shows the FT-IR spectra of (a) $Zn_4Al_{22}O_{37}$, (b) Ce^{3+}-activated $Zn_4Al_{22}O_{37}$, and (c) Eu^{3+}-activated $Zn_4Al_{22}O_{37}$. The absorption bands in the range 500–850 cm^{-1} correspond to the bending and stretching vibrations of the O—M—O and M—O bonds (where M = Zn,

Al, Ce, and Eu).[36] The absorption bands between 500 and 1000 cm^{-1} are related to the stretching and bending vibrations of the Al—O bonds.[37–39] The Al^{3+} ions located at octahedral sites of AlO_6 and tetrahedral AlO_4 denote the bending modes in the range 750–850 cm^{-1}. Zn^{2+} ions located at the centre of the ZnO_4 tetrahedral sites created the vibrations in between 500–750 cm^{-1}.[40] The absorption bands in between 500–750 cm^{-1} denoted the stretching and bending modes of the Al—O bonds in the octahedral coordination state.[38] The modes of stretching at 590 cm^{-1} were observed mainly due to the vibrations of three valence bonds with oxygen with octahedral locations.[41,42] The modes of stretching vibrations at 644 cm^{-1} were denoted the divalent ion bonded with oxygen atoms in the tetrahedral locations.[41,42] Stretching modes that corresponded to 590 cm^{-1} and 644 cm^{-1} were attributed to the T_{2g} modes and the vibrations at 420 nm were attributed to the E_g modes.[31] The modes of vibrations at the shoulder peak at 806 cm^{-1} occurred due to the Al—O bonds in the tetrahedral locations.[42,43]

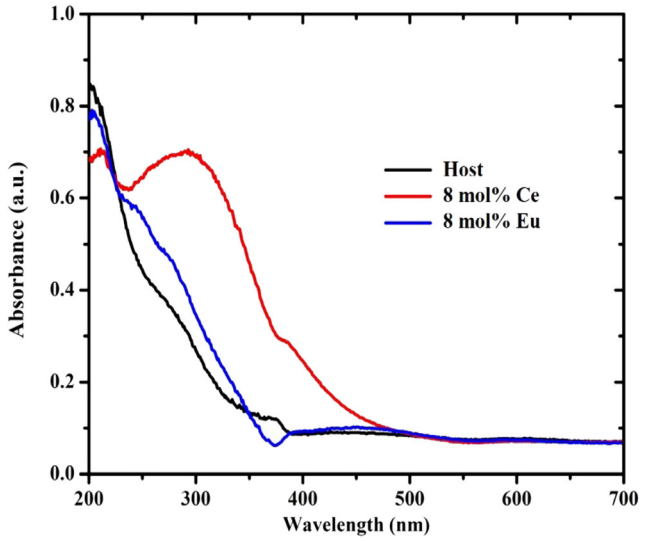

FIGURE 5 Ultraviolet–visible light absorbance spectra of the $Zn_4Al_{22}O_{37}$ host, Ce^{3+}-activated $Zn_4Al_{22}O_{37}$, and Eu^{3+}-activated $Zn_4Al_{22}O_{37}$

3.5 | Photoluminescence properties

3.5.1 | Luminescence of Ce^{3+}-activated $Zn_4Al_{22}O_{37}$

Ce^{3+} activators in the solid matrix exhibit the concentration-dependent luminescence properties of the host material. After particular concentration of the Ce^{3+} activators, quenching in the emission properties was carried out in the form of lattice vibrations. The quenching in the lumen output predicts that the Ce^{3+} ions pair comes closer to each other and dissipates the energy in terms of the phonons in the lattice. Therefore, the doping concentration of Ce^{3+} in the materials is one of the key factors to obtain the high light yield. To study the concentration-dependent luminescence properties, we varied the concentration of Ce^{3+} at 1 mol%, 2 mol%, 5 mol%, 8 mol%, and 10 mol% in the $Zn_4Al_{22}O_{37}$ matrix.

Figure 8 demonstrates the excitation spectrum of the Ce^{3+} (8 mol%)-activated $Zn_4Al_{22}O_{37}$ phosphor monitored under the 421 nm wavelength. The excitation spectrum denoted the broad band excitation peak at the 298 nm wavelength that ranged from 225 nm to 350 nm. The peak at 298 nm denoted the transition of 4f→5d in the Ce^{3+} ion. The PL emission characteristics of the Ce^{3+}-activated $Zn_4Al_{22}O_{37}$ phosphor were studied by monitoring the excitation wavelength at 298 nm (Figure 9). Ce^{3+} ions in the $Zn_4Al_{22}O_{37}$ matrix showed broad band luminescence at 421 nm. The lowest sublevels of 5d could be further split into different components due to the spin-orbit coupling. The Ce^{3+} broad band luminescence in the $Zn_4Al_{22}O_{37}$

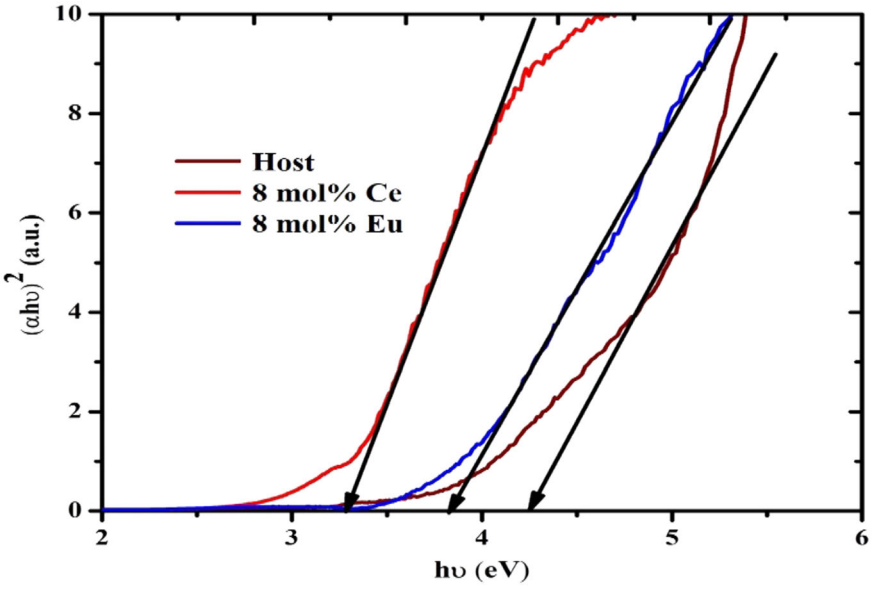

FIGURE 6 Optical band gap energies of the $Zn_4Al_{22}O_{37}$ host, Ce^{3+}-activated $Zn_4Al_{22}O_{37}$ and Eu^{3+}-activated $Zn_4Al_{22}O_{37}$ using a Tauc plot

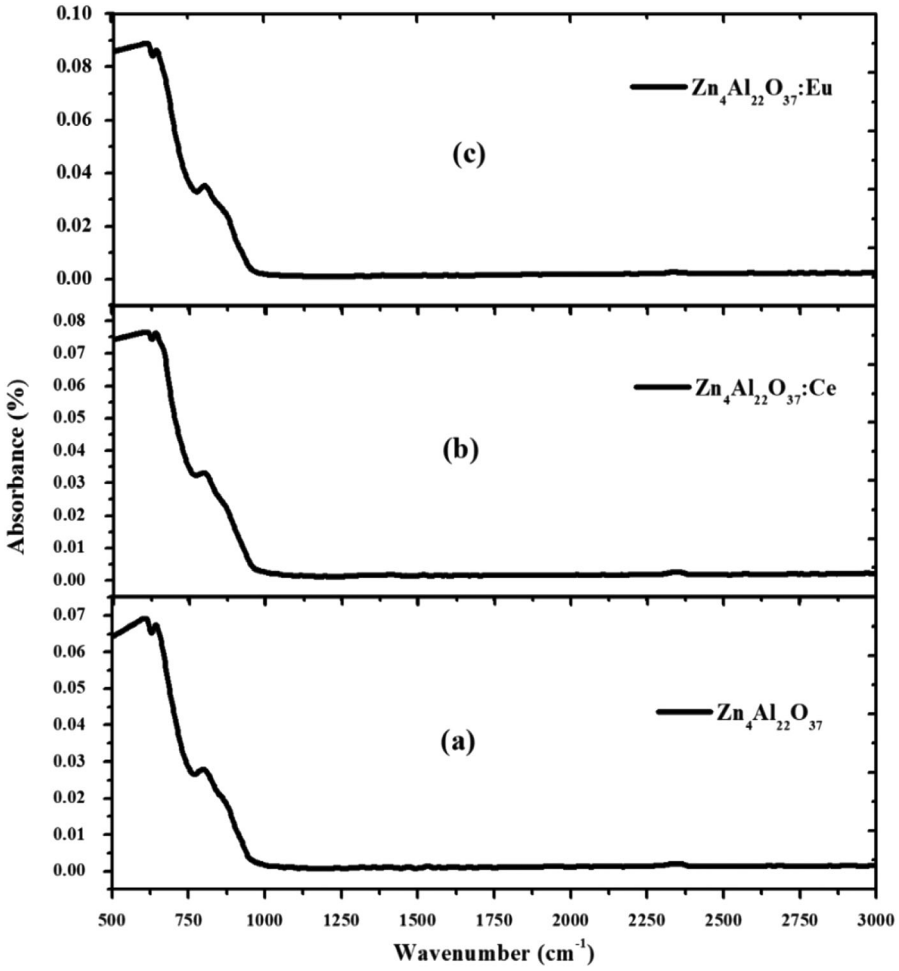

FIGURE 7 Fourier transform infrared spectra of (a) $Zn_4Al_{22}O_{37}$ host, (b) 8 mol% Ce^{3+}-activated $Zn_4Al_{22}O_{37}$ and (c) 8 mol% Eu^{3+}-activated $Zn_4Al_{22}O_{37}$

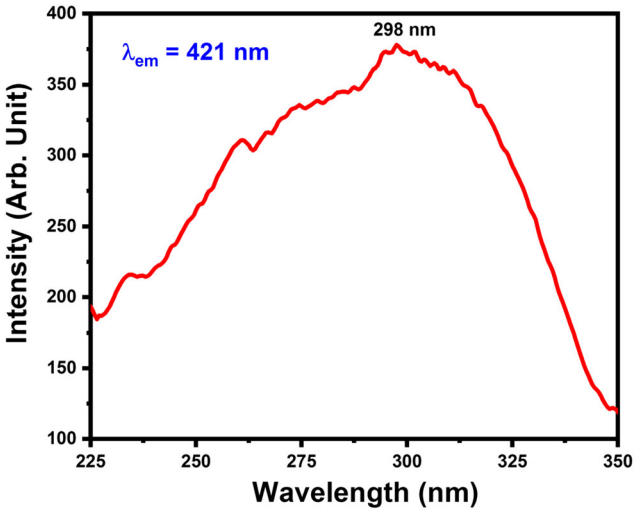

FIGURE 8 Photoluminescence excitation spectra of Ce^{3+}-activated $Zn_4Al_{22}O_{37}$ monitored under 421 nm emission

phosphor was due to the transitions from the lowest level 5d to the spin-orbit split of the 4f sublevels $^2F_{5/2}$ and $^2F_{7/2}$.[44–46] The emission from the Ce^{3+} centres was strongly influenced by the crystal field strength and the surrounding nature of the chemical bonding. The two doublet bands of the Ce^{3+} ions appeared for the lower (1 and 2 mol%) doping concentration of the Ce^{3+} ions in $Zn_4Al_{22}O_{37}$. The doublet bands merged into one broad band emission at 421 nm. Following the increase in doping concentration, the first peak at 405 nm shifted to 421 nm and for 8 mol% both peaks merged and resulted in one broad peak at 421 nm. Photoluminescence emission represented the increase in doping concentration of the Ce^{3+} ions in $Zn_4Al_{22}O_{37}$, increasing the intensity of emission up to 8 mol% doping concentration. Furthermore, it was observed that the emission intensity decreased when the concentration of Ce^{3+} ions was increased to more than 8 mol% (Figure 10), which might be possibly due to the concentration quenching (CQ) effect of luminescence. The CQ effect was caused by an excess of rare earth ions (Ce^{3+}). When the rare earth ions came closer to each other the absorbed energy was not utilized in terms of emission, but was transferred from one rare earth ion to the next. Therefore the emission became increasingly weaker. As the concentration of Ce^{3+} ions was increased, the distance between the Ce^{3+} ions decreased, therefore the intensity of the emission decreased.

Figure 11 denotes the Gaussian fitting curve of the Ce^{3+}-activated $Zn_4Al_{22}O_{37}$. The Gaussian fitting curve estimated two

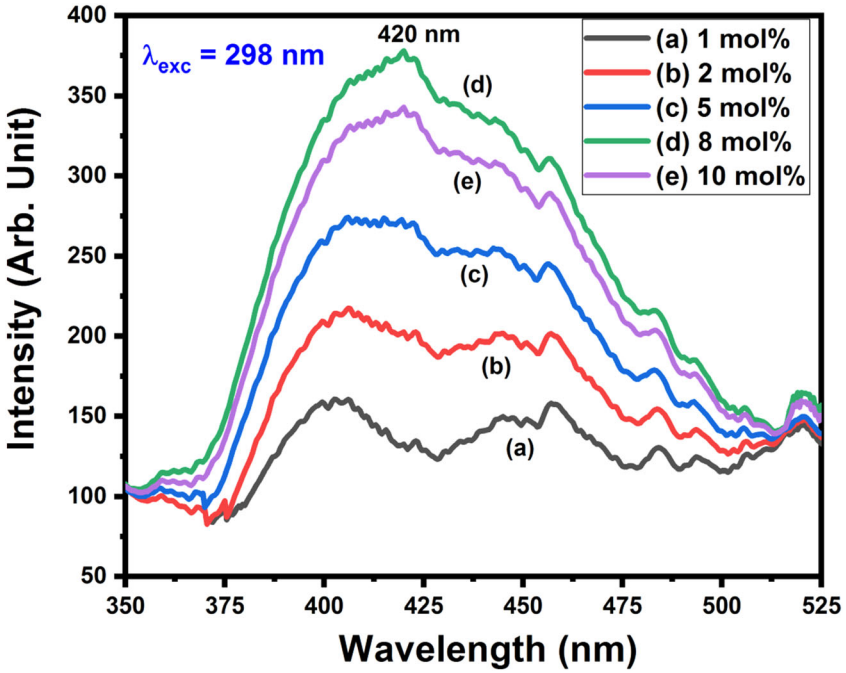

FIGURE 9 Photoluminescence emission spectra of Ce^{3+}-activated $Zn_4Al_{22}O_{37}$ monitored under 298 nm excitation

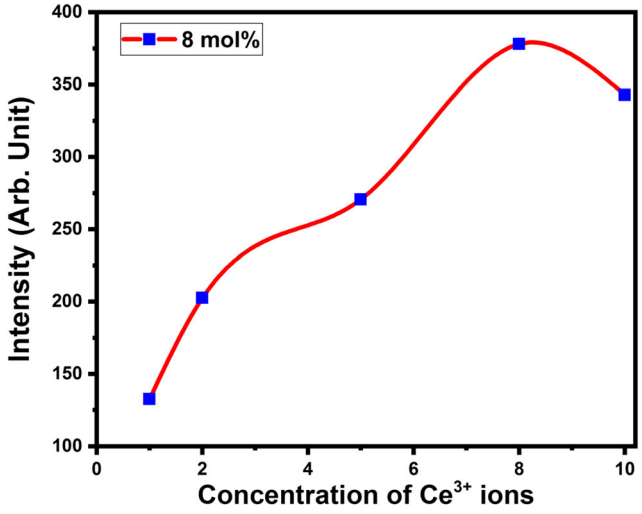

FIGURE 10 Variation in emission intensity with variation in the Ce^{3+} ions

emission peaks at 405 nm (24 691 cm^{-1}) and 466 nm (22 471 cm^{-1}) that corresponded to the 5d states of the $^2F_{5/2}$ and $^2F_{7/2}$ transitions of the Ce^{3+} ions, respectively. The energy level difference between two fitted peaks was observed at 2219 cm^{-1}, which was consistent with the 2000 cm^{-1} theoretical value.[47] A Stokes shift (ΔS) was observed at ~2580 cm^{-1} that was observed larger than that of the other Ce^{3+}-doped aluminates.[47] The Stokes shift increase was due to the Ce^{3+} ions that had been strongly attached to the surrounding ions in the host.[48]

The energy levels of the Ce^{3+} ions are illustrated in the schematic diagram in Figure 12(a). When the Ce^{3+}-activated $Zn_4Al_{22}O_{37}$ was excited by the 298 nm, the Ce^{3+} ions were excited to the 5d levels. These ions relaxed nonradiatively in the crystal and captured the lowest 5d state. The excited ions returned to the $^2F_{5/2}$ and $^2F_{7/2}$ sublevels of the 4f state by emitting the broad band emission. The ions relaxed to the 5d lower level from 5d higher levels using a multiphonon relaxation process.

3.5.2 | Eu^{3+} luminescence in $Zn_4Al_{22}O_{37}$

Eu^{3+}-activated phosphors exhibited different narrow peaks with different wavelengths and were 590–596 nm, 614–620 nm, 656–669 nm, and 689–701 nm, which corresponded to the $^5D_0 \rightarrow {}^7F_1$, $^5D_0 \rightarrow {}^7F_2$, $^5D_0 \rightarrow {}^7F_3$ and $^5D_0 \rightarrow {}^7F_4$ transitions, respectively. Eu^{3+} luminescence is very sensitive to the crystal field and surrounding molecules in the host. Figure 13 shows the PL excitation spectra of Eu^{3+}-activated $Zn_4Al_{22}O_{37}$ that was monitored under 594 nm emission. The maximum intensity peak was observed at 395 nm in the excitation spectrum due to $^7F_0 \rightarrow {}^5L_6$ transition. To study the concentration dependence of the luminescence, the concentrations of Eu^{3+} doping were varied and were 1 mol%, 2 mol%, 5 mol%, 8 mol% and 10 mol% in the $Zn_4Al_{22}O_{37}$ matrix.

The emission spectra of the Eu^{3+}-activated $Zn_4Al_{22}O_{37}$ phosphor were monitored under the wavelength 395 nm, as shown in Figure 14. The emission spectra of Eu^{3+}-activated $Zn_{4-x}Al_{22}O_{37}$ had two high intensity peaks at 594 nm and 614 nm. The peak at 594 nm was attributed to the $^5D_0 \rightarrow {}^7F_1$ transition. The transition $^5D_0 \rightarrow {}^7F_1$ denotes the Eu^{3+} ions acquired by the low symmetry sites in the crystal and corresponded to the magnetic dipole interactions.[49–53] The peak at 614 nm was assigned to the electronic transitions carried from $^5D_0 \rightarrow {}^7F_2$ in the Eu^{3+} ion. The transition $^5D_0 \rightarrow {}^7F_2$ was strongly correlated with the surrounding crystal field effect on the Eu^{3+} ions.[18,50]

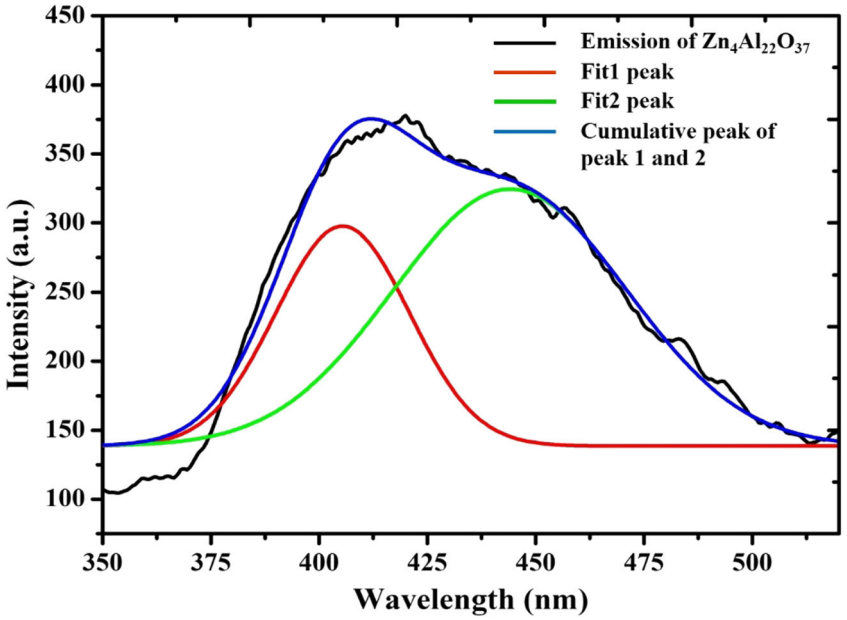

FIGURE 11 Gaussian fitting curve of emission spectra of Ce^{3+}-activated $Zn_4Al_{22}O_{37}$

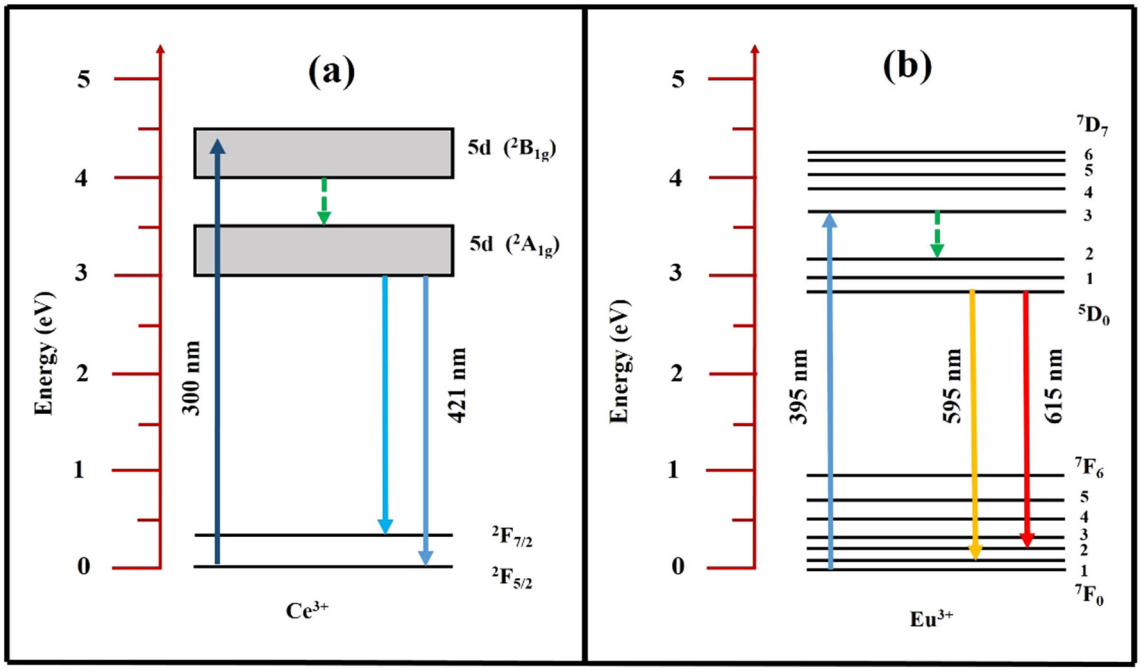

FIGURE 12 Energy level diagrams of (a) Ce^{3+} ions and (b) Eu^{3+} ions

Figure 15 shows the variation in emission intensity corresponding to different concentrations of Eu^{3+} ions. The emission intensity increased up to the 8 mol% concentration, at more than this concentration the emission intensity decreased due to the CQ effect. There was no shift of wavelength due to change in doping concentration, but intensity variation only was observed. Therefore these phosphors may be applicable for the orange/red emissions.

The energy levels of the Eu^{3+} ions are illustrated in Figure 12(b). The Eu^{3+} ions absorbed radiation when excited by 395 nm wavelength radiation and is shown by the blue arrow in the energy level diagram. After relaxation in 5d levels, there were two transitions at wavelengths 594 nm and 614 nm. The transition at 594 nm was attributed to the $^5D_0 \rightarrow {}^7F_1$ change and the transition at 614 nm was due to the $^5D_0 \rightarrow {}^7F_2$ change

3.6 | Colour coordinates

The colour coordinates (x, y) were determined using a radiant imaging colour calculator program that refers to the 1931 Commission

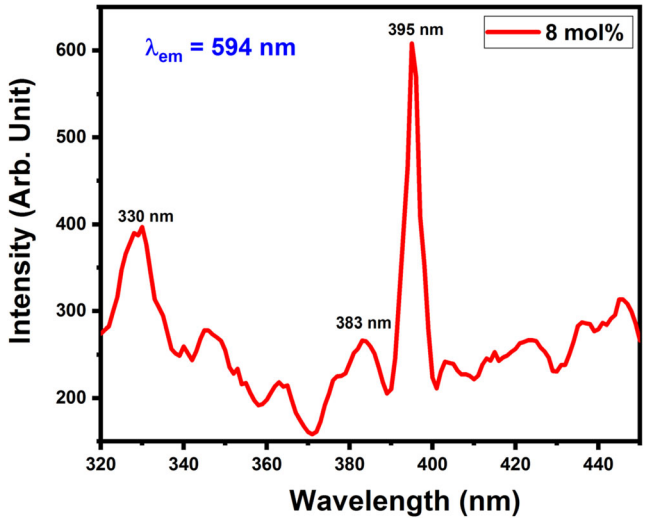

FIGURE 13 Photoluminescence excitation spectra of Eu^{3+}-activated $Zn_4Al_{22}O_{37}$ monitored under 594 nm emission

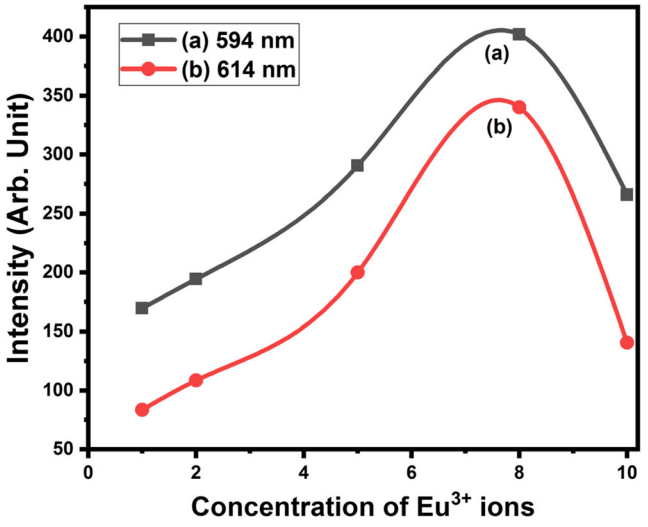

FIGURE 15 Variation in emission intensity with variation in the Eu^{3+} ions

FIGURE 14 Photoluminescence emission spectra of Eu^{3+}-activated $Zn_4Al_{22}O_{37}$ monitored under 395 nm excitation

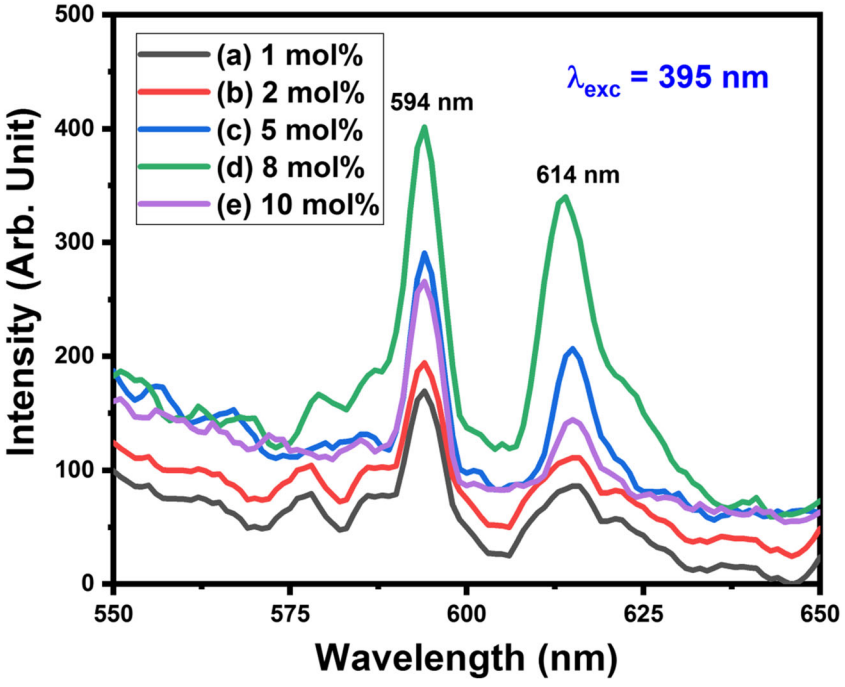

Internationale de l'Eclairage (CIE) standard source [illuminants Cs (0.3101, 0.3162)].[54,55] The colour coordinates were estimated using the following relationships:[56]

$$x = \frac{X}{X+Y+Z}, y = \frac{Y}{X+Y+Z} \text{ and } z = \frac{Z}{X+Y+Z} \quad (7)$$

Equation 7 denotes the three tristimulus values X, Y, and Z for a colour with spectral power distribution P(λ) and these values could be calculated using Equation 8:

$$X = \int_{\lambda_1}^{\lambda_2} P(\lambda)\,\bar{x}(\lambda)\,d\lambda, X = \int_{\lambda_1}^{\lambda_2} P(\lambda)\,\bar{x}(\lambda)\,d\lambda \text{ and } Y = \int_{\lambda_1}^{\lambda_2} P(\lambda)\,\bar{y}(\lambda)\,d\lambda \quad (8)$$

where λ_1 to λ_2 is the wavelength range of the PL emission spectrum, $\bar{x}(\lambda)$, $\bar{y}(\lambda)$, and $\bar{z}(\lambda)$ are three colour matching functions; and the wavelength of equivalent monochromatic light is λ. The estimated colour coordinates of Ce^{3+}-activated $Zn_4Al_{22}O_{37}$ for the 8 mol% concentration were x = 0.1567, y = 0.0637 (blue) at 420 nm emission, as shown in Figure 16 by point A. The corresponding tristimulus coordinates of Ce^{3+}-activated $Zn_4Al_{22}O_{37}$ were estimated also and these were

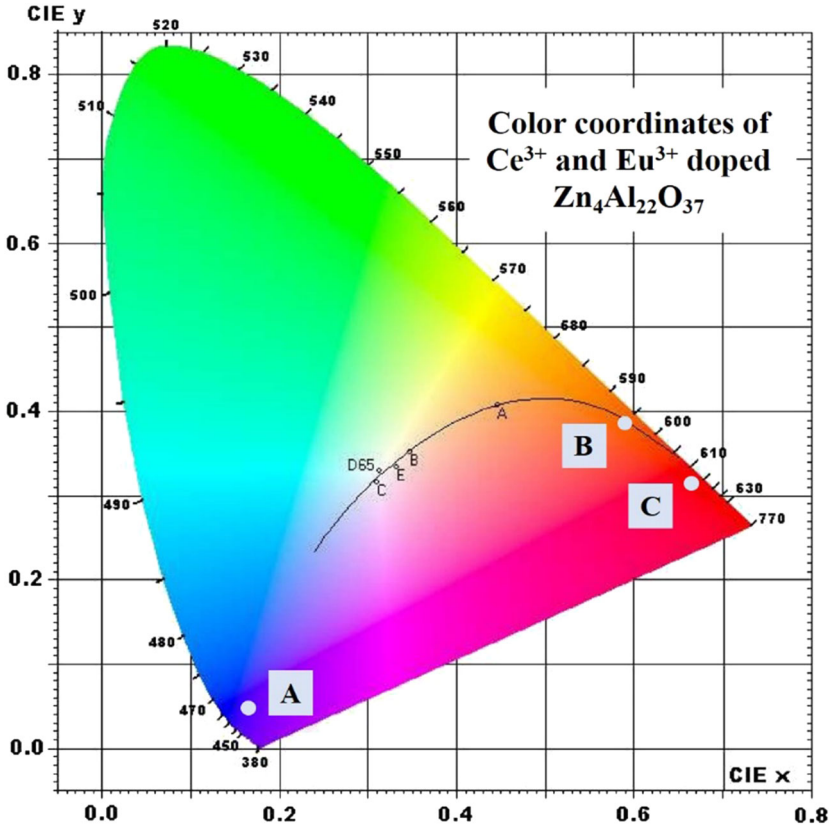

FIGURE 16 Colour coordinates of Ce^{3+}-activated $Zn_4Al_{22}O_{37}$ and Eu^{3+}-activated $Zn_4Al_{22}O_{37}$

X = 6.66, Y = 4.07 and Z = 0.01. The estimated colour coordinates of Eu^{3+}-activated $Zn_4Al_{22}O_{37}$ for the 8 mol% concentration were x = 0.6018, y = 0.3976 (orange) at 594 nm and x = 0.6779, y = 0.3219 (red) at 614 nm as shown in Figure 16 by points B and C respectively. The corresponding tristimulus coordinates for Eu^{3+}-activated $Zn_4Al_{22}O_{37}$ were X = 7.38, Y = 4.88, Z = 0.01 (orange) and X = 8.71, Y = 4.14, Z = 0.00 (red).

4 | CONCLUSION

Ce^{3+}- and Eu^{3+}-activated $Zn_4Al_{22}O_{37}$ phosphors were successfully prepared using solution combustion synthesis and their structural, morphological, and luminescence properties were investigated. XRD showed the hexagonal structure of the prepared $Zn_4Al_{22}O_{37}$ host, Ce^{3+}-activated $Zn_4Al_{22}O_{37}$ and Eu^{3+} activated $Zn_4Al_{22}O_{37}$. HR-TEM measurements showed the nanocrystalline nature of the particles. Ce^{3+}-activated $Zn_4Al_{22}O_{37}$ phosphor produced blue emission at 421 nm (5d→4f) under the 298 nm excitation. Under 395 nm excitation, the Eu^{3+}-activated $Zn_4Al_{22}O_{37}$ phosphor produced showed emission at 594 nm ($^5D_0 \rightarrow {}^7F_1$) and 614 nm ($^5D_0 \rightarrow {}^7F_2$). Luminescence intensity increased with variation in doping concentration and the 0.8 mol% concentration was observed as the optimum concentration. The colour coordinates of Ce^{3+}- and Eu^{3+}-activated $Zn_4Al_{22}O_{37}$ confirmed that these phosphors may be useful for UV absorption and visible light emission lighting applications.

ORCID

Dinesh S. Bobade https://orcid.org/0000-0003-4960-4772
Yatish R. Parauha https://orcid.org/0000-0002-7968-3160

REFERENCES

[1] C. M. Mehare, Y. R. Parauha, N. S. Dhoble, C. Ghanty, S. J. Dhoble, *J. Mol. Struct.* **2020**, *1212*, 127957.
[2] Q. He, C. Hu, *Opt. Mater.* **2014**, *38*, 286.
[3] Y. R. Parauha, V. Chopra, S. J. Dhoble, *Mater. Res. Bull.* **2020**, *131*, 110971.
[4] P. Wang, X. Xu, J. Qiu, X. Yu, Q. Wang, *Opt. Mater.* **1826**, *2014*(11), 36.
[5] C. R. García, L. A. Diaz-Torres, J. Oliva, G. A. Hirata, *Opt. Mater.* **2014**, *37*, 520.
[6] S. Li, X. Peng, X. Liu, Z. Huang, *Opt. Mater.* **2014**, *38*, 242.
[7] C. Ronda, *WILEY-VCH Verlag GmbH & Co*, KGaA, Weinheim **2008**.
[8] S. J. Dhoble, Vijay B. Pawade, Hendrik C. Swart & V. Chopra Elsevier Ltd., 2020
[9] C. Peng, G. Li, D. Geng, M. Shang, Z. Hou, J. Lin, *Mater. Res. Bullet.* **2012**, *47*(11), 3592.
[10] S. Menon, B. Dhabekar, E. A. Raja, S. P. More, T. K. G. Rao, R. K. Kher, *J. Lumin.* **2018**, *128*, 673.
[11] D. Zhang, C. Wang, Y. Liu, Q. Shi, W. Wang, Y. Zhai, *J. Lumin.* **2012**, *132*, 1529.
[12] G. E. Malashkevich, M. Melnichenko, E. Poddenezhny, A. A. Boiko, *J. Non-Cryst. Solids.* **1999**, *260*, 141.
[13] H. Bi, W. Cai, L. Zhang, *Mater. Res. Bull.* **2000**, *35*, 1495.
[14] R. Reisfeld, H. Minti, A. Patra, D. Ganguli, *M. Gaft* **1998**, *54*, 2143.
[15] K. A. Gedekar, S. P. Wankhede, S. V. Moharil, R. M. Belekar, *J. Mater. Sci.: Mater. Elect.* **2018**, 294466.
[16] G. N. Nikhare, S. C. Gedam, S. J. Dhoble, *J. Lumin.* **2013**, *137*, 290.

[17] V. Singh, J. Zhu, V. Natarajan, **2006**, *203*, 2058.
[18] W. B. Dai, M. Zhou, Z. Y. Xian, L. K. Zeng, *RSC Adv.* **2014**, *4*, 25470.
[19] G. Li, T. Long, Y. Song, G. Gao, J. Xu, B. An, S. Gan, G. Hong, *J. Rare Earth* **2010**, *28*, 22.
[20] Y. R. Parauha, S. J. Dhoble, *Luminescence* **2010**, 2.
[21] J. H. Kim, *Phys. B: Phys. Cond. Matter.* **2016**, *505*, 52.
[22] M. T. Tsai, Y. X. Chen, P. J. Tsai, Y. K. Wang, *Thin Solid Films* **2010**, *518*, 9.
[23] X. Y. Chen, C. Ma, Z. J. Zhang, B. N. Wang, *Mater. Sci. Eng.* **2008**, *B151*, 224.
[24] G. Rani, *Powder Technol.* **2017**, *312*, 354.
[25] P. Kumari, Y. Dwivedi, *J. Lumin.* **2016**, *178*, 407.
[26] M. Kumar, S. K. Gupta, *J. Lumin.* **2015**, *168*, 151.
[27] V. Singh, R. P. S. Chakradhar, J. L. Rao, D.-K. Kim, *J. Lumin.* **2008**, *128*, 394.
[28] M. Zawadzki, J. Wrzyszcz, W. Strek, D. Hreniak, *J. Alloys Compd.* **2001**, *323*, 279.
[29] W. Strek, P. Dereń, A. Bednarkiewicz, M. Zawadzki, J. Wrzyszcz, *J. Alloys Compd.* **2008**, *300-301*, 456.
[30] D. P. Dutta, R. Ghildiyal, A. K. Tyagi, *J. Phys. Chem. C* **2009**, *113*, 16954.
[31] R. Khenata, M. Sahnoun, H. Baltache, M. Rérat, A. H. Reshak, Y. Al-Douri, B. Bouhafs, *Phys. Lett. A* **2005**, *344*, 271.
[32] S. Mathur, M. Veith, M. Haas, H. Shen, N. Lecerf, V. Huch, S. Hüfner, R. Haberkorn, H. P. Beck, M. Jilavi, *J. Am. Ceram. Soc.* **2001**, *84*, 1921.
[33] M. Kumar, V. Natarajan, S. V. Godbole, *Bull. Mater. Sci.* **2014**, *37*, 1205.
[34] J. Tauc, A. Menth, *J. Non-Crys. Solids.* **1972**, *8*, 569.
[35] D. L. Wood, J. Tauc, *Phys. Rev. B* **1972**, *5*, 3144.
[36] M. A. Subhan, T. Ahmed, P. Sarker, T. T. Pakkanen, M. Suvanto, M. Horimoto, H. Nakata, *J. Lumin.* **2014**, *148*, 98.
[37] S. F. Wang, G. Z. Sun, S. F. Wang, L. M. Fang, L. Lei, X. Xiang, X. T. Zu, *Sci. Repor.* **2015**, *5*, 12849.
[38] D. L. Ge, Y. J. Fan, C. L. Qi, Z. X. Sun, *J. Mater. Chem.* **2013**, *A1*, 1651.
[39] I. B. Huang, Y. S. Chang, H. L. Chen, C. C. Hwang, C. J. Jian, Y. S. Chen, M. T. Tsai, *Thin Solid Films* **2014**, *570*(301), 451.
[40] S. Janakov, L. Salavcova, G. Renaudin, Y. Filinchuk, D. Boyer, P. Boutinau, *J. Phys. Chem. Solids* **2007**, *68*(5–6), 1147.
[41] H. A. Mohammed, R. A. Rasool, *Raf. J. Sci.* **2019**, *28*(3), 33.
[42] V. M. Grošev, M. Vrankić, A. Maksimović, V. Mandić, *J. Alloys Compd.* **2017**, *697*, 90.
[43] T. Tangcharoen, J. T. Thienprasert, C. Kongmark, *Mater. Sci.* **2020**.
[44] X. He, X. Liu, R. Li, B. Yang, K. Yu, M. Zeng, R. Yu, *Sci. Report.* **2016**, *6*, 22238.
[45] Z. Pan, W. Li, Y. Xu, Q. Hu, Y. Zheng, *RSC Advan.* **2016**, *6*, 20458.
[46] A. Selot, M. Aynyas, M. Tiwari, K. Dev, *AIP Conf. Procee.* **2016**, *1728*, 02026.
[47] X. Zhang, B. Park, N. Choi, J. Kim, G. C. Kim, J. H. Yoo, *Mater. Lett.* **2009**, *63*, 700.
[48] V. B. Pawade, N. S. Dhoble, S. J. Dhoble, *Solid State Sci.* **2012**, *14*, 607.
[49] D. S. Bobade, Y. R. Parauha, S. J. Dhoble, P. B. Undre, *Optik* **2021**, *227*, 166119.
[50] V. B. Pawade, S. J. Dhoble, *Solid State Sci.* **2012**, *14*(5), 607.
[51] H. Liu, Y. Hao, H. Wang, J. Zhao, P. Huang, B. Xu, *J. Lumin.* **2011**, *131*(11), 2422.
[52] J. Kaur, Y. Parganiha, V. Dubey, *Phys. Res. Intern.* **2013**, 494807, 1.
[53] D. S. Bobade, P. B. Undre, *Integr. Ferroelectr.* **2020**, *205*, 72.
[54] K.N. Shinde, S.J. Dhoble, H.C. Swart, K. Park, *Springer*, **2012**.
[55] Color calculator version 2, A Software from Radiant Imaging, Inc., **2007**.
[56] J. Yang, B. Chen, E. Y. Bun Pun, B. Zhai, H. Lin, *J. Lumin.* **2013**, *134*, 622.

FWHM, full width half maximum.

How to cite this article: D. S. Bobade, Y. R. Parauha, S. J. Dhoble, P. B. Undre, *Luminescence* **2022**, *37*(3), 500. https://doi.org/10.1002/bio.4200